nature materials

SUPPLEMENTARY INFORMATION

DOI: 10.1038/NMAT3597

Nanoscale spin reversal by non-local angular momentum transfer following ultrafast laser excitation in ferrimagnetic GdFeCo

Introduction

This supplementary material is provided in support of the main paper with details not possible to include therein. It is divided into two main sections; *section 1* encompasses the technical details of the experiment and data analysis, while *section 2* provides additional experimental data and analysis omitted from the main paper.

In *section 1.1* we detail the experimental setup used at the SXR beamline of the Linac Coherent Light Source. This is followed by *section 1.2* detailing the sample preparation and the x-ray characterization performed at beamline 13-3 of the Stanford Synchrotron Radiation Lightsource. In *section 1.3* we detail how spin sensitivity is achieved in resonant x-ray scattering and subsequently in *section 1.4* the methodology of data analysis.

The additional experimental data presented in *section 2* begins with *section 2.1* where we present spatially averaging time-resolved X-ray Magnetic Circular Dichroism (XMCD) data taken concurrently with the scattering data presented in the main paper. *Section 2.2* discusses how the XMCD and scattering data relate to different lengthscales of magnetization, while *section 2.3* discusses the magnitude of the change of magnetization in the nanoscale Gd and Fe (chemically) enriched regions discussed in the main paper.

DOI: 10.1038/NMAT3597

1. Supplementary Experimental Information.

1.1 Experimental setup

The measurements were carried out at the SXR beamline *(1)* of the Linac Coherent Light Source (LCLS) *(2)* using the RCI end station. A grating monochromator selected the photon energy with a resolution of 0.5 eV *(1)*. The x-ray beam was focused to a 70 µm spot size at the sample, resulting in x-ray fluences below 2 mJ/cm^2. Circularly polarized x-rays were generated using the preferential absorption of one helicity in magnetic transmission thin films. At the Gd M_5-edge we used a 260 nm thick out-of-plane magnetized $Fe_{73}Gd_{27}$ film at normal x-ray incidence, and at the Fe L_3-edge a 40 nm thick in-plane magnetized Fe film at 30^o grazing incidence was used. Both polarizing films were placed in a beamline section where a large x-ray spot generated negligible beam damage. This resulted at the respective absorption edges in 60% and 44% circularly polarized x-ray beams *(3)*. Optical pump laser pulses, with a wavelength of 800 nm and duration of 50 fs (upon compression), were propagated collinear to the x-ray beam with a focus size on the sample of 160 µm. After correction for the electron bunch arrival time jitter *(2),* the remaining optical - x-ray temporal jitter was determined to 150 fs (FWHM) *(4)*. Diffraction patterns were detected by two low-noise p–n junction charge-coupled device (pnCCD) detectors, usually operated in the CFEL-ASG Multi-Purpose (CAMP) instrument *(5)*. Data were accumulated at a repetition rate of 20 Hz with magnetic field pulses of alternating field direction applied along the sample normal to reset the sample magnetization before each pump-probe event (the external field was off during the measurement events). Another key feature of the pnCCD detector is the ability to pass the direct beam through a central hole in the detector and monitor the x-ray intensity ($I_{\pm}(q=0)$ see section 2.1) with an avalanche photo diode.

1.2. Sample growth & characterization

The studied samples were identical to those used in ref. *(8)* of the main paper. Thick amorphous 30 nm thin films of $Gd_{24}Fe_{66.5}Co_{9.5}$ were deposited by magnetron sputtering on a free-standing Si_3N_4 membrane of 100 nm thickness. To avoid oxidation of the $Gd_{24}Fe_{66.5}Co_{9.5}$ layer, a 10 nm capping layer of Si_3N_4 was deposited on top of the film. Films exhibited an out-of-plane magnetic anisotropy as deduced from magnetic hysteresis measurements.

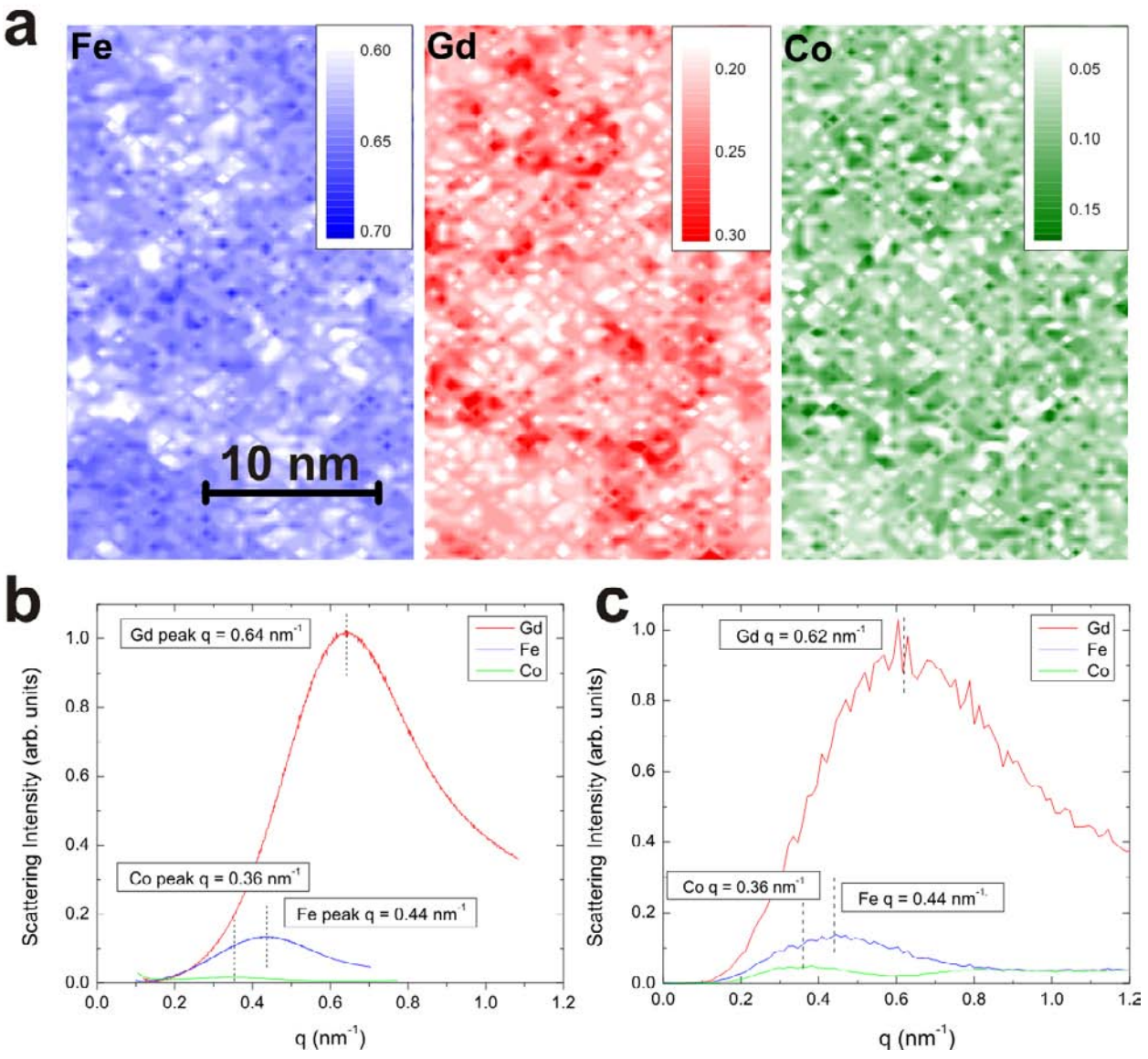

Fig. S1: ***a****. Simulated elemental maps for Fe, Gd and Co for a 30x20 nm region. Gd and Fe tend to segregate into anti-correlated enriched regions, while Co fills the remaining voids in the distribution.* ***b****. Angle-integrated resonant x-ray scattering data at the Gd (M5), Fe (L3), & Co (L3) edges, and* ***c*** *The same scattering patterns as calculated from the simulated distribution as shown in* ***a****. The simulated patterns reproduce the key features of the scattering: the scattering peak positions of the three elements and their relative intensities.*

DOI: 10.1038/NMAT3597

An ideally amorphous alloy should be homogeneous at all length scales, with no chemical variations that would produce diffraction. However, the nanoscale structure of *amorphous* alloys is generally more complex *(6,7)*. The microstructure of the GdFeCo films was chemically and magnetically characterized at beamline 13.3 of the Stanford Synchrotron Radiation Light Source (SSRL). Fig. S1b shows typical radial diffraction scans obtained with the x-ray energy tuned into resonance between core and valence shells. For Gd the x-ray energy is tuned to the M_5 absorption edge at 1190eV, for Fe the L_3 edge at 707 eV, and for Co the L_3 edge at 778 eV. The scattering from Gd and Fe show diffuse rings, each at a well defined momentum transfer q. As the scattering shows no radially directional structure, the intensity is angle integrated around the q = 0 point. Intensity peaks in this scattering are observed to correspond to lengthscales of $\zeta=2\pi/q$~10 nm for Gd, ~14 nm for Fe and ~18 nm for Co (given by the diffraction peak maxima in Fig. S1b).

We conclude that our nominally amorphous samples are stoichiometrically inhomogeneous at the few nm lengthscale. The q values of the scattering peaks are associated with the lengthscales of the stoichiometric fluctuations and are seen to be different for each of the constituent elements. The shortest fluctuations are associated with Gd, the largest atomic species (atomic diameter of Gd = 0.22 nm), while longer periods are associated with the smaller, lighter Fe and Co atoms (diameter of Fe = 0.16 nm & Co = 0.15 nm). Thermodynamic considerations suggest that several intermetallic crystal phases can exist in the Gd-Fe-Co system *(8)*; however, our data suggests no evidence of microcrystalline order. The data suggests local chemical enrichment over ~10 nm lengthscales by growth inhomogeneity and subsequent interdiffusion of the chemical species. This is consistent with the amorphous structures observed in Gd–Fe *(9)*, and Gd–Co *(10)* systems.

A model of the amorphous structure was constructed to reproduce the scattering data. To model the strong scattering peaks at different positions for Gd, Fe and Co it was necessary to introduce local chemical reordering within the sample. The model considered reordering by a process of chemical migration over short distances ~ 6.4 nm, while maintaining the film's density and thickness. In this process Gd and Fe tend to segregate into enriched regions, while Co fills remaining gaps. To reproduce the experimentally observed q peaks, the average migration distances are adjusted such that average displacement of Fe (~7.1 nm) is greater than the average

displacement of Co (6.4 nm), which is greater than the average displacement of Gd (5.7 nm). The average displacement is approximately associated with a half period of the observed scattering length ζ ($\zeta = 2\pi/q$). Fig. S1a shows elemental density maps of the three elements generated by the model, while figure S1b & c show the measured and simulated charge scattering intensities.

Samples with the same nominal concentration and thickness ($Gd_{24}Fe_{66.5}Co_{9.5}$) were also grown on Ted Pella 8 nm Si_3N_4 grid membranes suitable for analysis with transmission electron microscopy (TEM). Elemental mapping was performed with an energy-dispersive x-ray (EDX) detector in scanning transmission electron microscopy (STEM) mode with a probe size of ~1nm. Maps were taken in 1 nm steps for 20x50 pixels, with a 5 second dwell time, and ~300 cts/second (in total, across all energies). The Fe K-edge, Gd L-edge, and Co K-edge were used in the EDS spectrum for quantification. The measured maps for each energy are shown in Fig. 1 of the main paper. Gd rich areas are indicated by red shading in Fig. 2 and Fig. 3 of the main paper, while the Fe rich areas are represented by blue shading. The chemical segregation observed is identical in form to our model, however, the concentration changes with STEM-EDX data are approximately twice that observed on the samples with x-ray scattering. This difference is attributed to growth differences on the different substrates.

Further analysis of the magnetic scattering and TEM microscopy data indicates that the sample shows distinct areas of strong Gd enrichment (~20% coverage of the total sample) and areas of Fe enrichment (~40% coverage of the total sample). The Co fluctuations show only weak correlation in the scattering, while the elemental microscopy shows no correlation above 1 nm. Both the model simulation and TEM microanalysis indicate that the concentration fluctuations are similar in size for all three elements. The average regional concentration changes were determined from modeling of the scattering intensity, and are given in Table 1 below.

Region	Enrichment Area	% Relative Conc. Increase
Gd enrichment	0.2	5.1%
Fe enrichment	0.4	1.9%

Table 1: Average concentration changes in the $Gd_{24}Fe_{66.5}Co_{9.5}$ sample.

DOI: 10.1038/NMAT3597

1.3. Spin-sensitivity in small-angle scattering

Resonant x-ray scattering can be split into two well-defined contributions: the material's electronic charge distribution and its magnetic polarization. For simplicity we refer to these as charge and magnetic scattering. The scattering angle is defined by the momentum transfer vector q. The intensity pattern in q space is related to the Fourier transform of the real space distributions. The two largest contributions to the resonant scattering factor have been derived by Hannon *et. al. (11)*:

$$F^{\pm} = F_C\, \mathbf{e}\cdot\mathbf{e'} - iF_S\, \mathbf{e} \times \mathbf{e'}\cdot\mathbf{m} \qquad (1)$$

where **e** and **e'** are the polarization vectors of incident and scattered x-rays, **m** is the unit magnetization vector in the sample and $F_{C,S}$ are the atomic charge/magnetic scattering factors.

For circularly polarized x-rays, with angular momentum (anti)aligned with the sample magnetization along the incidence direction, this expression becomes:

$$F_q^{\pm} = C_q\, e^{-i\varphi} \pm S_q\, e^{-i\gamma} \qquad (2)$$

Where C_q and S_q are defined as Fourier amplitudes of the real-space charge and magnetic distributions, and the complex part of the scattering factors and the propagation phase has been incorporated into a single phase term. Now the scattering intensity can be expressed as:

$$I_{\pm}(q) = C_q^2 + S_q^2 \pm 2C_q\, S_q\, cos(\varphi - \gamma) \qquad (3)$$

In the $I_{\pm}(q)$ distribution from GdFeCo, the charge term dominates the magnetic term at all lengthscales and $I_{\pm}(q)$ can be approximated by:

$$I_{\pm}(q) = C_q^2 \pm 2C_q\, S_q \qquad (4)$$

Two simplifications are made between equations (3) and (4). First, the S_q^2 term is neglected; this is permissible as $C_q \gg S_q$ over the entire q range (see Fig. S2). Often the S_q^2 term cannot be

neglected and may in fact dominate in certain situations, for example at the q vector corresponding to the magnetic domain period in Co/Pt multilayers *(12)*. In this case, to retrieve quantifiable information from the interference term, S_q^2 must be included. Second, the phase of the interference term, $\cos(\phi-\gamma)$, is taken as being equal to one. This assumption asserts that only spatially correlated areas of charge and magnetic variation contribute to the scattering interference term. In the diffuse scattering limit where individual speckles are too small or too numerous to be resolved on the detector - as is the case in this experiment - the oscillating constructive–destructive interference from uncorrelated charge and magnetic scattering averages to zero (namely, the $\cos(\phi-\gamma)$ term oscillates between +1 and -1). Therefore, only correlated areas of charge and magnetic variation with a well-defined, fixed phase relationship (constant $\cos(\phi-\gamma)$) contribute to the interference term. We note that in this notation the Fourier amplitudes C_q and S_q are real numbers but can still be positive or negative as they measure the deviation of charge and spin *distributions* from the sample average values.

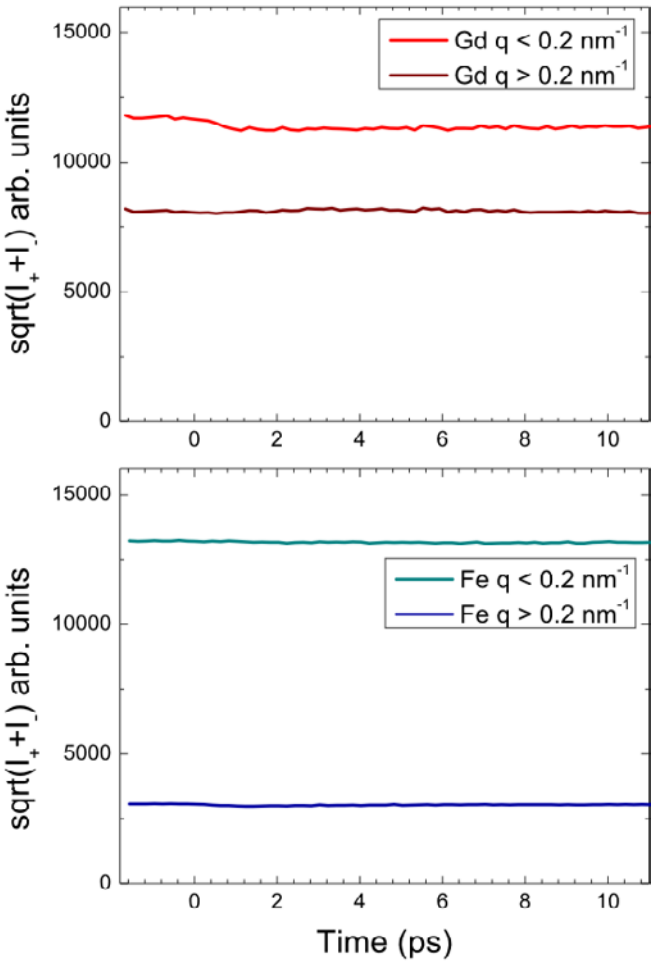

Fig. S2: High-q and low-q Gd (top panel) and Fe (bottom panel) scattering intensity, sqrt(I^++I^-)=2(C_q^2+S_q^2), vs. time delay. The small variations due to S_q^2 magnetic scattering are negligible compared to C_q^2 charge scattering.

DOI: 10.1038/NMAT3597

1.4. Data processing

The diffracted intensity is recorded with a 2D CCD detector developed specifically for single-shot x-ray detection. All recorded diffraction patterns are circularly symmetric about the $\boldsymbol{q} = 0$ forward scattering direction, and can therefore be angularly integrated. Diffraction patterns are individually binned by the laser – x-ray (pump–probe) time delay and the applied magnetic field direction. Finally, angular integrations of intensity are calculated and normalized to the incident x-ray intensity.

The separation of change and magnetic contributions from the collected data is illustrated in Fig. 1b of the main text. The integrated scattering intensity is shown for $I_+(q)$ and $I_-(q)$. Using equation 2, the charge and magnetic Fourier amplitudes C_q and S_q are determined.

2. Supplementary Experimental Data.

This section details additional experimental data and analysis conducted in support of the results in the main paper. It is first useful to mention the context of our experiment with respect to previous work on GdFeCo. The complexity of laser-induced spin dynamics in this material is well documented and previous work has focused on the all-optical switching regime (*13,14* and ref. (*8*) and *(9)* from the main paper). In this intermediate switching regime, it is difficult to separate true non-equilibrium dynamics from coherently driven dynamics, such as the inverse Faraday effect *(15),* relativistic mechanisms *(16)* and conventional dynamics as governed by the Landau Lipshitz Gilbert equation (*17,18*). To avoid this complexity and focus on the general non-equilibrium dynamics of angular momentum, we excite the system with an energy sufficient to destroy all magnetic order. Therefore, the laser fluence used was 24 mJ/cm^2, significantly higher than that used to observe transient ferromagnetism 4.4 mJ/cm^2 (ref. *(8)* from the main paper), or all-optical switching of 2.9 mJ/cm^2 *(13)*. We note that for the laser fluence 24 mJ/cm^2 the equilibrium sample temperature after 1-2 ps will be above the magnetic ordering temperature.

2.1. Time-resolved X-ray Magnetic Circular Dichroism

X-ray Magnetic Circular Dichroism (XMCD) is used to measure the spatially averaged magnetization within a material (see ref. *(8)* from the main paper). It can also be viewed as diffraction or scattering, but for the specific case of $q = 0$ (zero momentum transfer). XMCD data (Fig. S3) were collected by means of a photodiode placed behind the 2D pnCCD detector. A gap between the pnCCD detector plates allowed XMCD data to be collected concurrently with scattering data.

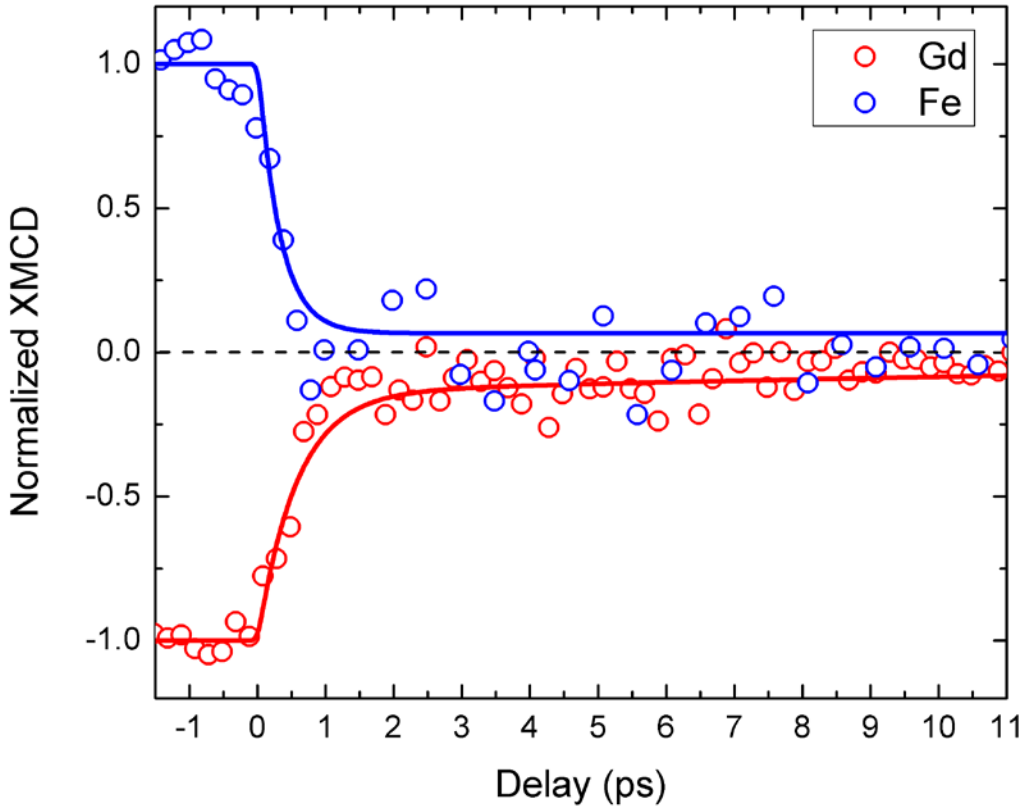

Fig. S3: Time resolved XMCD measured concurrently with scattering data for Gd (red) and Fe (blue). Solid lines show normalized fits to scattering data at $q < 0.2$ nm^{-1}.

DOI: 10.1038/NMAT3597

2.2. Magnetic Lengthscales and Scattering

The magnetic scattering from different lengthscales, which therefore contribute at different scattering vector q values, can be attributed to different physical origins. Essentially, S_q (derived from the interference term) is the Fourier transform of the spatial magnetic distribution sampled by the charge scattering C_q. Here we distinguish diffracted intensity from three different length scales, labeled (a), (b) and (c) in Fig. S4. In *region (a)*, the lengthscale corresponds to the sample size (or explicitly the area probed by the x-ray beam); here the S_q signal is dominated by the average film magnetization. This is the region probed in XMCD measurements (see ref. *(8)* of the main paper). *Region (b)* is characterized by lengthscales of order ~100 nm. Here, the S_q signal is dominated by thickness variations in the film and artifacts of the growth process. It is important to note that the time-dependent behavior of S_q in this region correlates with the average film magnetization (see Fig. S3) probed in *region (a)*. *Region (c)* is characterized by lengthscales associated with stoichiometric chemical inhomogeneity. This lengthscale is associated with the strong charge scattering ring, which peaks at $2\pi/q = 10$ nm for Gd. Here, the negative sign of S_q is characteristic of anti-correlation between charge and magnetic scattering, which will be further elaborated in the next section.

It is instructive to compare the contributions of *regions (a-c)* given by XMCD and magnetic scattering, respectively. XMCD data ($I_{\pm}(q=0)$) were collected simultaneously with scattering data during the experiment. An identical temporal behavior is observed for XMCD and low-q regions as shown in Fig. S3.

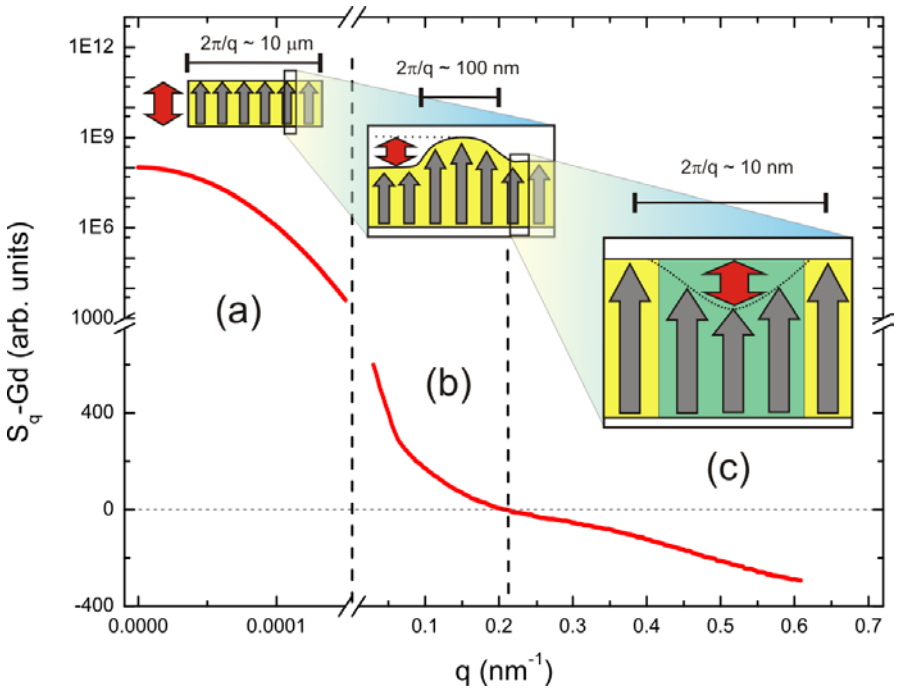

Fig. S4: The real-space origins of S_q. Red lines show experimental data for Gd (sign convention reversed with respect to main paper) based on the 2D scattering data (regions b and c, referred to as low-q and high-q regions, respectively) in the main paper, and the XMCD data presented in Fig. S3 (region a). A gaussian lineshape has been assumed for the XMCD – region (a) – contribution. Scale breaks and a log-y scale are used in region (a) due to the large spectral weight associated with q = 0. The insets illustrate the origins of magnetic variation for the respective regions, as explained in the text. Gray arrows represent the size of the magnetic moments as a function of one spatial coordinate. Red double arrows denote the amplitude of the magnetic moments' spatial variation (i.e. the Fourier component S_q). In regions (a) and (b), the chemical composition is homogeneous (marked as yellow shades) while for region (c) <10nm size Gd rich regions (green shading, see Fig. S1) have reduced magnetic moments.

The negative sign of S_q in region (c) is due to an anti-correlation of charge and magnetic distributions, as S_q is derived from the product C_qS_q (see section 1.3). This indicates either an increasing Gd magnetization in regions with lower Gd content (something precluded) or a lower

DOI: 10.1038/NMAT3597

Gd magnetization in regions of Gd enrichment. This latter case that occurs within GdFeCo. While seemingly counterintuitive, the local out-of-plane magnetization will cant into the plane (effectively reducing the measured out-of-plane component) due to the effects of anisotropy, which is highly dependent on local pair correlations *(19)*. More extreme versions of this effect are well known in other rare-earth – transition metal alloys where they lead to such effects as *sperimagnetism (20)*.

2.3. Estimation of Transient Gd & Fe Magnetization

In this section we explain the details of the fitting of the magnetic distribution and the estimate of the weight factors γ_{Fe} and γ_{Gd} for the real-space magnetic changes in the respective Fe and Gd enriched regions. These factors give the local change in the magnetization with respect to the sample average within these enriched regions. This information is contained within the S_q-Fe and S_q-Gd distributions in the high-q regions. To determine the real-space magnetic deviations we extend the model for the charge scattering developed in section 1.2.

As mentioned in section 1.3, the charge–magnetic interference term is only non-zero for diffuse scattering when the charge and magnetic distributions are correlated. The magnetic distribution is therefore intimately related to the charge distribution. Here we assume the simplest case: that the magnetic distribution is linearly related to the charge distribution:

$$M_\lambda(x,y) = \bar{M}_\lambda + \alpha_\lambda \Delta C_\lambda(x,y) \qquad (5)$$

Where: λ = Gd or Fe, α is a constant and $\Delta C_\lambda(x,y) = \left(C_\lambda(x,y) - \bar{C}_\lambda\right)/\bar{C}_\lambda$.

The most trivial case of the above model is uniform correlation between magnetic and charge scattering: that out-of-plane magnetization of Gd or Fe will increase linearly with the number of atoms. This case is shown as a dotted line in Fig. S5. The scattering from the trivial case shows a peak in S_q; however, the sign of S_q is opposite that observed in the experiment for both Gd and

Fe. To reproduce the experimental results, it is necessary that $\alpha < 0$; namely, that the charge and magnetic distributions are anti-correlated.

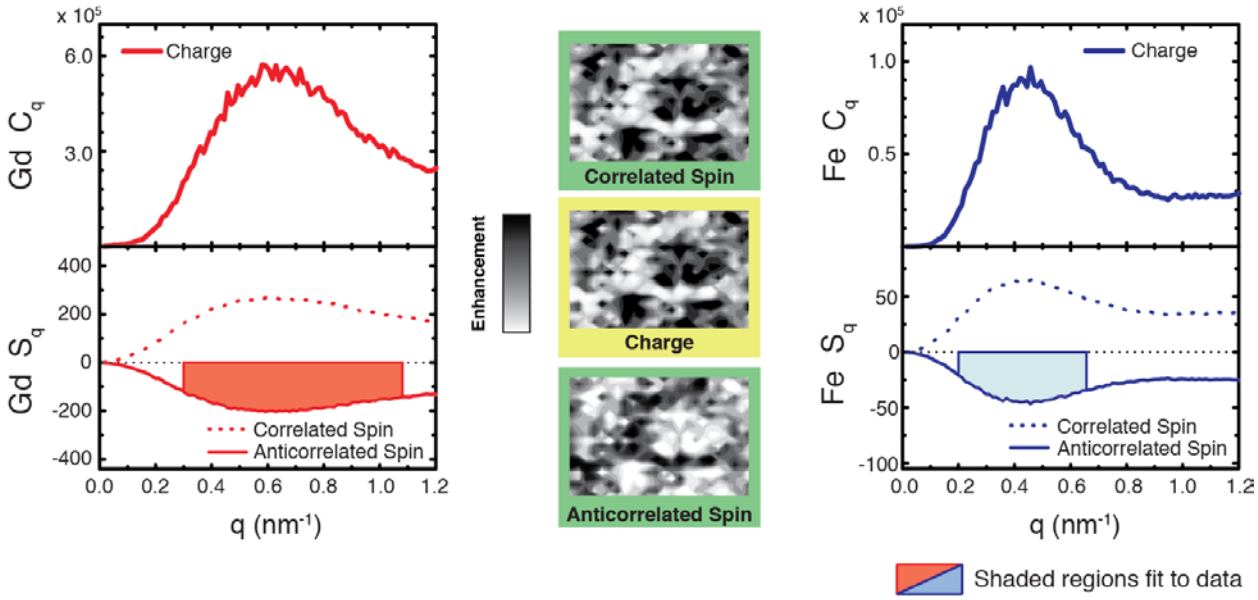

Fig. S5: Model simulations of the charge and magnetic scattering. The model illustrates how the reversal of the sign observed in S_q at $q > 0.2$ nm^{-1} is characteristic of the anti-correlation of the nanoscale charge and magnetic textures. The size of the magnetic deviations is found by fitting the scattering intensities in the model to the measurement data. (Note: the sign convention used above is such that the average magnetization is directed in the positive S_q direction).

The value of α is determined by matching S_q in the simulation to the measured data. This is done in two steps. First, equilibrium measurements of S_q made at SSRL supplement the S_q data taken at LCLS, and a region is defined encompassing the peak in S_q (shaded in Fig S6 for Gd). Second, the integral of S_q in this region is matched to the identical region of the model (shaded region in Fig. S5). For the time-resolved data, it is assumed that changes in the shaded region that are observed experimentally are representative of the total intensity change. It is therefore determined in equilibrium ($t < 0$) that $\alpha_{Gd} = -229\ \mu_B/nm^3$ and $\alpha_{Fe} = -85\ \mu_B/nm^3$.

DOI: 10.1038/NMAT3597

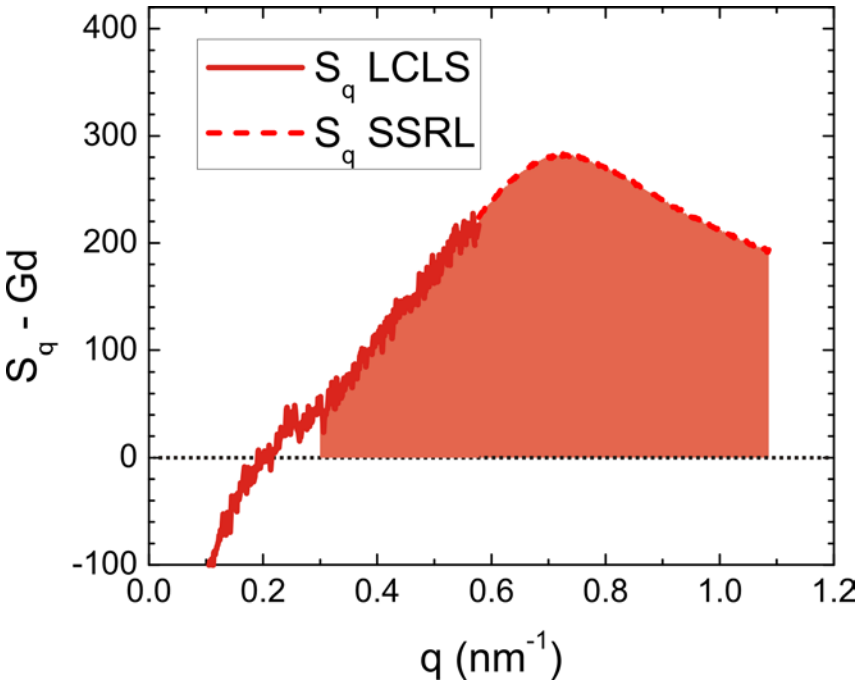

Fig. S6: Equilibrium Sq for Gd. Extended region measured at SSRL. Shaded area is used as the scaling parameter for the model shown in Fig S5 above. (Note sign convention for Sq taken from main paper—M_{avg}(Gd) in negative direction.)

The average real-space change in the enriched regions is given by $\gamma = \alpha\Delta C_{av}$. For Gd enriched regions $\Delta C_{av}^{Gd}(Gd-rich) = 0.034$, while for Fe enriched $\Delta C_{av}^{Fe}(Fe-rich) = 0.013$; this gives γ_{Gd}(Gd-rich) = -7.8 μ_B/nm^3 or -9.6% change from the average M_{Gd}, and γ_{Fe} = -1.1 μ_B/nm^3 or -2.0% change from the average M_{Fe} (further changes detailed in table 2 below). These values serve as the normalization for the local magnetization plot shown in Fig. 4c of the main paper.

Gamma /Region	*Gd-enriched (area = 18%)*	*Fe-enriched (Area = 42%)*
$\gamma_{Gd} = \alpha\Delta C_{av}$	-7.8 μ_B/nm^3	+2.7 μ_B/nm^3
$\gamma_{Fe} = \alpha\Delta C_{av}$	+0.41 μ_B/nm^3	-1.1 μ_B/nm^3

Table 2: Gamma values for the Gd- and Fe-enriched regions of GdFeCo.

Bibliography

1. Heimann, P. *et al.* Linac Coherent Light Source soft x-ray materials science instrument optical design and monochromator commissioning. *Rev. Sci. Instrum.* **82,** 093104 (2011).

2. Emma, P. *et al.* First lasing and operation of an angstrom-wavelength free-electron laser. *Nature Photon.* **4**, 641 (2010).

3. Pfau, B. *et al.* Magnetic imaging at linearly polarized x-ray sources. *Opt. Express* **18**, 13608 (2010).

4. Gahl, C. *et al.* A femtosecond X-ray/optical cross correlator. *Nature Photon.* **2**, 165 (2008).

5. Strüder, L. *et al.* Large-format, high-speed, X-ray pnCCDs combined with electron and ion imaging spectrometers in a multipurpose chamber for experiments at 4th generation light source. *Nucl. Instrum. Methods Phys. Res.* **A614**, 483 (2010).

6. Samwer, K., Fecht, H.J. & Johnson, W.L. *Glassy Metals III. Topics in Applied Physics*, Vol. 72, (Springer-Verlag, Berlin Heidelberg, 1994).

7. O'Handley, R.C. Physics of ferromagnetic amorphous alloys. *J. Appl. Phys.* **62,** R15 (1987).

8. Liu, Z.-K., Zhang, W. & Sundman, B. Thermodynamic assessment of the Co-Fe-Gd systems. *J. Alloys Compd.* **226,** 33 (1995).

9. Lee, S.R. & Miller, A.E. Crystallization behavior of evaporated Gd-Fe alloy films. *J. Appl. Phys.* **55**, 3465 (1984).

10. Hoffmann, H., Owen, A.J. & Schröpf, F. Electron microscopy of evaporated and sputtered Gd/Co and Ho/Co films. *Phys. Stat. Sol. (a)* **52**, 161 (1979).

11. Hannon, J.P., Trammell, G.T., Blume, M. & Gibbs, D. X-Ray resonance exchange scattering. *Phys. Rev. Lett.* **61**, 1245 (1988).

12. Kortright, J.B. *et al.* Soft-x-ray small-angle scattering as a sensitive probe of magnetic and charge heterogeneity. *Phys. Rev. B* **64**, 092401 (2001).

13. Stanciu, C.D. *et al.* All-Optical magnetic recording with circularly polarized light. *Phys. Rev. Lett.* **99,** 047601 (2007).

14. Vahaplar, K. *et al.* Ultrafast path for optical magnetization reversal via a strongly nonequilibrium state. *Phys. Rev. Lett.* **103**, 117201 (2009).

15. Stanciu C.D. *et al.* Ultrafast interaction of the angular momentum of photons with spins in the metallic amorphous alloy GdFeCo. *Phys. Rev. Lett.* **98,** 207401 (2007).

16. Bigot, J.-Y., Vomir, M. & Beaurepaire, E. Coherent ultrafast magnetism induced by femtosecond laser pulses. *Nature Phys.* **5**, 515 (2009).

DOI: 10.1038/NMAT3597

17. Stanciu, C.D. *et al*. Ultrafast spin dynamics across compensation points in ferromagnetic GdFeCo: The role of angular momentum compensation. *Phys. Rev. B* **73**, 220402 R (2006).

18. Kirilyuk, A., Kimel, A. & Rasing, Th. Ultrafast optical manipulation of magnetic order. *Rev. Mod. Phys.* **82**, 2731 (2010).

19. Taylor, R.C. & Gangulee, A. Magnetic anisotropy in evaporated amorphous films of the ternary system $Gd_x(Fe_{1-y}Co_y)_{1-x}$. *J. Appl. Phys.* **48,** 358 (1977).

20. Coey, J.M.D. Amorphous magnetic order. *J. Appl. Phys.* **49,** 1646 (1978).